Composition-driven changes in lattice sites occupied by indium solutes in Ni_2Al_3 phases

Matthew O. Zacate and Gary S. Collins*
Department of Physics, Washington State University, Pullman, Washington 99164-2814, USA
(Received 18 August 2003; revised manuscript received 29 March 2004; published 6 July 2004)

Lattice locations of dilute indium solute atoms in phases having the Ni_2Al_3 crystal structure were determined using the technique of perturbed angular correlations of γ rays. Four sites, including two inequivalent group IIIA sites, a group VIII site, and an empty-lattice site, were distinguished by measurement of nuclear quadrupole interactions at $^{111}In/Cd$ probes in the phases Ni_2Ga_3, Pt_2Ga_3, Ni_2Al_3, Pd_2Al_3, and Pt_2Al_3. Occupied sites were identified by comparison with quadrupole interactions of probes in three indides having the same structure, Ni_2In_3, Pd_2In_3, and Pt_2In_3, and by calculations of electric-field gradients at the four sites. Probes were observed to "switch" sites as the composition changed from being rich to poor in the transition metal (TM). Indium was observed to exclusively occupy one of the group III sites in TM-rich gallides and aluminides. In TM-poor gallides, indium occupied the TM sublattice, while near the stoichiometric composition it also partially occupied the empty-lattice site, which has interstitial character. For TM-poor aluminides, highly inhomogenous quadrupole interactions were observed indicating that indium was located on irregular sites in lattice sinks such as grain boundaries. Dependences of site fractions on composition are interpreted using a thermodynamic model that relates fractions of solutes on substitutional, interstitial, and lattice-sink sites to concentrations of intrinsic defects. Heuristic rules are presented which describe site-selection behavior based on the experiments and model. Among other rules, it was found that there is a maximum tendency for solutes to occupy interstitial sites near the stoichiometric composition.

DOI: 10.1103/PhysRevB.70.024202 PACS number(s): 61.72.Ss, 61.72.Ji, 61.18.Fs, 82.60.Lf

I. INTRODUCTION

There is considerable interest in lattice locations of solutes in intermetallic compounds because of their effects on material properties. A variety of methods has been applied to measure site occupations of solutes, including x-ray diffraction,[1] ALCHEMI,[2] and hyperfine interaction probe methods.[3,4] Site occupations have been found to change with composition or temperature, so that one cannot simply expect a one-to-one correspondence exists between a solute and a site. In this situation, experiments with unrecognized differences in sample preparation and composition may lead to conflicting results. This makes it useful to formulate heuristic rules for site-selection behavior based on the thermodynamics of solutions and supported by case studies in interesting systems. Previous investigations have focused on compounds having simple crystal structures such as B2 and $L1_2$ because of their great number and technological importance (see, e.g., Ref. 1). These structures have just one substitutional site for each host element. Structures having inequivalent sites for host elements or the possibility of interstitial site occupation may exhibit new site preference phenomena.

In the present work, we investigate lattice locations of indium solutes in five phases having the Ni_2Al_3 structure. The structure has two inequivalent Al-type sites, one Ni-type site, and an empty sublattice site. Lattice locations were determined by measuring quadrupole interaction signals characteristic of each site, with signal amplitudes proportional to the fractions of solute in each location. The signals arise from precessions of nuclear quadrupole moments in crystal electric-field gradients (efg's), measured using perturbed angular correlation spectroscopy (PAC). $^{111}In/Cd$ probe atoms acted as the solutes and had mole fractions of order 10^{-8}, so that site preference behavior was observed in the dilute solute limit. Four distinct site preferences were observed: Solutes strongly preferred to occupy one of the two inequivalent sublattices of a host element. As the composition changed from being rich to deficient in a host element, site occupations were observed to switch from the substitutional site of one element to the substitutional site of the other element, to an interstitial site, or to sites in "lattice sinks" such as grain boundaries or dislocations. The observed behaviors are interpreted with the aid of a thermodynamic model.

The paper is organized as follows. First, the crystal structure is described and results of point-charge calculations of efg's are given that are used to help identify the sites. Next, sample preparation and PAC methods are described, followed by the experimental results. A thermodynamic model for the site occupation of solutes is then developed which is used to interpret the results. The model demonstrates an intimate connection between site-selection behavior and intrinsic defect concentrations. A set of heuristic rules for site-selection and site-switching behavior are formulated, many of which are illustrated by the measurements. Implications of the experimental results and model are discussed in the final section. In the Appendix, a thermodynamic model is presented for defects and solutes in the Ni_2Al_3 structure starting from the Gibbs free energy of the crystal. Brief accounts have appeared elsewhere of some experimental results[5] and of the thermodynamic model as applied to a different crystal structure.[6]

II. CRYSTAL STRUCTURE AND ELECTRIC-FIELD GRADIENTS

A. Crystal structure

Compounds having the Ni_2Al_3 structure[7–9] ($D5_{19}$, Pearson symbol hP5, space group $P\bar{3}m1$) are formed from eight out

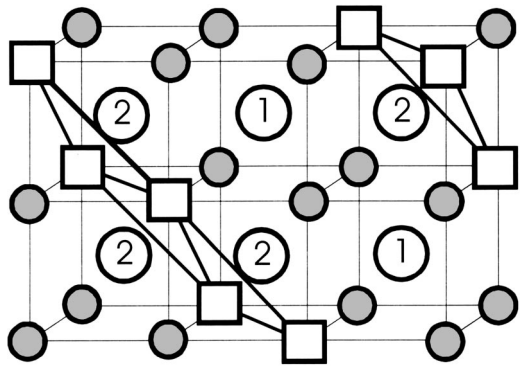

FIG. 1. Ni_2Al_3 crystal structure referenced to related CsCl structure. The transition-metal site α is shown by small shaded circles, the two trivalent-metal sites β_1 and β_2 by larger open circles, and empty sublattice sites τ by squares.

of nine combinations of group VIII metals Ni, Pd, and Pt with group IIIB elements Al, Ga, and In. The phases are well ordered and the structure is closely related to the CsCl structure. Binary systems Ni-Al, Ni-Ga, and Pd-In have neighboring CsCl phases with extended fields that include compositions of less than 50 at. % of the transition metal, for which the deviation from stoichiometry is known to be accommodated by vacancies on the transition-metal sublattice.[10] The vacancies act as structural point defects and are located more or less at random. Heuristically, the Ni_2Al_3 structure (written generically as A_2B_3 below) forms when the A vacancies in A poor CsCl phases condense on every third 111 plane.[7,9] At the stoichiometric composition, every third A-type plane is empty.

The structure has four sublattices: one A-atom sublattice α, two inequivalent B-atom sublattices β_1 and β_2, and the empty sublattice τ that in the related CsCl phase would be occupied by A atoms. The sublattices have numbers of sites in the proportions $N_\alpha:N_{\beta 1}:N_{\beta 2}:N_\tau=2:1:2:1$. The crystal structure is shown in Fig. 1 in a cubic approximation described below. Trivalent atom sites β_1 and β_2 are indicated by numbered circles, the transition-metal site α by small shaded circles, and the empty site τ by squares.

Table I lists measured x-ray lattice parameters, axial ratios c/a, and fractional coordinates z of lattice planes along the reference 111 direction.[8,11] Also listed are unit-cell volumes Ω of the A_2B_3 phases, found to be slightly less than equivalent volumes of the corresponding equiatomic CsCl phases (three unit cells). c/a ratios are reduced by a few percent below the "ideal" value $\sqrt{3/2}$ for the cubic structure by contraction along the 111 direction normal to the empty planes. Relaxations of atom positions within the unit cell from values for the cubic structure are similarly small. Thus, the "parent" cubic structure shown in Fig. 1 is an excellent approximation to the actual structure.[12]

To investigate how volumes of the sites might influence solute site preferences, Wigner-Seitz volumes were determined numerically for the eight phases using structural data in Table I. Volumes of vacant sites were partitioned among neighboring occupied sites in the calculations. The site volumes obtained are listed in Table II and can be compared with the volume of an indium atom in indium metal, 18.0×10^{-3} nm^3. It can be seen that indium solutes are oversized for all sites in the aluminides and gallides, with site β_2 providing the closest match among the three substitutional sites. Thus, one can expect site β_2 to be preferred by indium solutes over site β_1, as is confirmed below in the experiments. Additional calculations were carried out in which the volume of the empty site was computed in the same way as the host-element sites. These calculations showed that Wigner-Seitz volumes of the four sites α, β_1, β_2, and τ remained very close to each other. The τ site thus has an available volume comparable to volumes of the other sites and can be thought of as an interstitial site with a large volume.

B. Electric-field gradients

Local configurations of the four sites are shown in the cubic approximation in Fig. 2. Transition-metal and empty sites α and τ are each surrounded by cubes of eight trivalent atoms. Trivalent sites β_1 and β_2 have, respectively, six and five A atoms in the first neighbor shell, with remaining sites vacant. Independent of the small structural contractions and relaxations, all four sites retain threefold site symmetry about

TABLE I. Lattice parameters of A_2B_3 phases having the Ni_2Al_3 structure, including fractional coordinates z along the c axis for A-type site α and B-type site β_2 ($z[\beta_1]\equiv 0$ and $z[\tau]\equiv 0.5$). Also listed are unit-cell volumes Ω and, where available, three times the unit-cell volume of the neighboring CsCl phase.

Phase	a (nm)	c (nm)	c/a	$z[\alpha]$	$z[\beta_2]$	$\Omega=a^2c/2\sqrt{3}$ (nm^3)	3Ω(CsCl) (nm^3)
ideal CsCl			1.2247($=\sqrt{3/2}$)	0.167	0.667		
Ni_2Al_3	0.404	0.490	1.213	0.149	0.648	0.0693	0.07215
Pd_2Al_3	0.422	0.516	1.223	0.149	0.648	0.0796	
Pt_2Al_3	0.421	0.517	1.228	0.160	0.630	0.0794	
Ni_2Ga_3	0.405	0.490	1.210	0.138	0.625	0.0696	0.07257
Pt_2Ga_3	0.422	0.517	1.225	0.160	0.633	0.0797	
Ni_2In_3	0.439	0.530	1.207	0.135	0.641	0.0885	0.08928
Pd_2In_3	0.452	0.549	1.215	0.138	0.625	0.0971	0.10395
Pt_2In_3	0.453	0.551	1.216			0.0979	

TABLE II. Volumes of Wigner-Seitz cells of substitutional sites calculated using experimental lattice parameters. For comparison, the volume of an In atom is 18.0×10^{-3} nm^3.

Phase A_2B_3	$\Omega=\sqrt{3}a^3c/2$ (10^{-3} nm^3)	$V(\alpha)$ (10^{-3} nm^3)	$V(\beta_1)$ (10^{-3} nm^3)	$V(\beta_2)$ (10^{-3} nm^3)
Ideal CsCl[a]	(1.00)	0.176	0.200	0.224
Ni_2Al_3	69.2	12.1	14.2	15.4
Pd_2Al_3	79.5	14.0	16.4	17.6
Pt_2Al_3	79.3	14.0	16.3	17.5
Ni_2Ga_3	69.9	12.3	14.5	15.4
Pt_2Ga_3	80.4	14.2	16.6	17.7
Ni_2In_3	87.3	15.1	17.9	19.6
Pd_2In_3	97.8	17.2	20.2	21.6
Pt_2In_3	97.8	17.2	20.1	21.6

[a]Assuming no contraction or relaxation: $c/a=\sqrt{3/2}$, $z[\beta_2]=2/3$, and $z[\alpha]=1/6$.

the 111 direction normal to the empty planes. In this situation, the electric-field gradient tensor is axially symmetric (asymmetry parameter $\eta=0$) and is determined by a single parameter, the principal component of the efg tensor V_{zz}, called simply the efg below. The efg at a site is given by a sum over contributions from external charges q_i at distances r_i that make angles θ_i with respect to the symmetry axis:

$$V_{zz}=\sum_i q_i\frac{3\cos^2\theta_i-1}{r_i^3}. \tag{1}$$

efg's at the four sites were calculated using Eq. (1) by lattice sums with point charges assigned to each sublattice site. This simple point-charge approximation has been found to be useful for predicting relative efg's, although estimation of absolute values would require a more sophisticated treatment of the electronic structure.

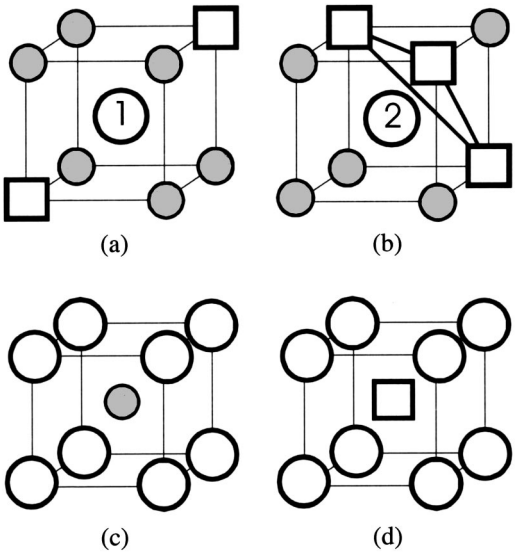

FIG. 2. Local environments of the four sites in the Ni_2Al_3 structure drawn in a cubic approximation: (a, b) trivalent-element sites β_1 and β_2; (c) transition-metal site α; and (d) empty sublattice site τ.

Due to the r^{-3} dependence in Eq. (1), the efg is strongly affected by contributions from the closest atomic shell. As shown in Fig. 2, local configurations of sites α and τ are cubic, for which it can be found from Eq. (1) that V_{zz} is zero. On the other hand, large efg's are expected for the noncubic configurations of sites β_1 and β_2. Consideration of the local configurations therefore leads one to expect that efg's for sites β_1 and β_2 calculated by summation over the entire crystal will be much larger than for sites α and τ.

Expectations based on the local configurations were confirmed by summations over large volumes. The sums depend on effective charges of the two kinds of host atoms and of the vacancy. Such charges arise through charge transfer between atoms, for which the semiempirical model of Miedema and co-workers[14] provides a simple conceptual picture.[15] Let us define effective charges of A atoms, B atoms, and the vacant sites as q_A, q_B and q_V, respectively. Then, owing to overall charge neutrality of the compound, one has $2q_A+3q_b+q_V=0$. There are thus two independent effective charges, which can be taken to be q_A and q_V. While efg's at different sites depend on the two charges, ratios of efg's depend only on the ratio of charges. This fact simplifies comparison between the efg calculations and quadrupole interaction measurements reported below because a signal was observed in each of the eight phases that could be attributed to probe atoms on the β_2 sublattice. Accordingly, results of the lattice sum calculations are presented in Fig. 3 in the form of curves showing how the ratios of efg's at sites α, β_1, and τ to the efg at site β_2 vary as a function of the effective charge ratio q_A/q_V.

In the calculations leading to Fig. 3, efg's were calculated by summing Eq. (1) over spherical volumes containing up to $\sim10^6$ atoms centered on the site of interest. Summations converged as the volume of summation increased, with final uncertainties estimated to be of order 1%. efg's were insensitive to precise values of the axial ratio and planar relaxations, with results in Fig. 3 obtained using lattice parameters of Pd_2In_3 taken from Table I. Absolute values of ratios of efg's of sites α, β_1, and τ to the efg of site β_2 are drawn as

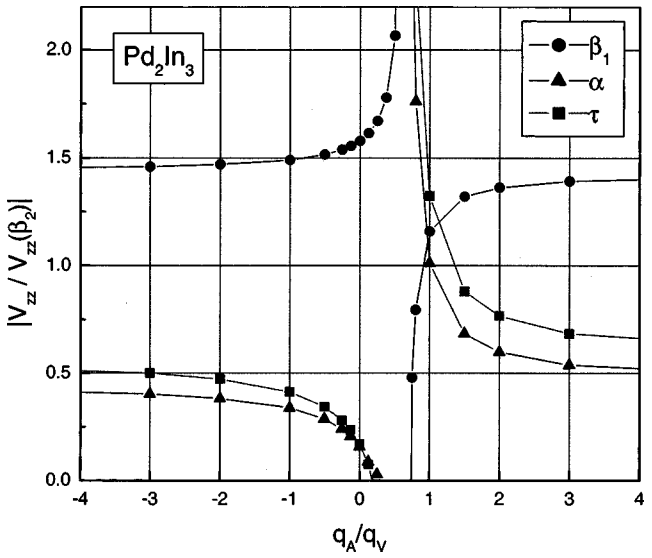

FIG. 3. Electric-field gradients at β_1, α, and τ sites in Ni_2Al_3 structure, normalized to the efg at the β_2 site, plotted vs the ratio of effective charges of A atoms on the α sublattice and vacancies on the τ sublattice. The experimental ratio $\omega_1(\beta_1)/\omega_1(\beta_2) \cong 1.6$ observed for three indides indicates a charge ratio $q_A/q_V \approx +0.1$.

functions of q_A/q_V. Apart from a domain close to $q_A/q_V = +0.645$, at which efg values diverge owing to an accidental zero of $V_{zz}(\beta_2)$, it can be seen that $|V_{zz}(\beta_1)|$ is roughly 1.5 times greater in magnitude than $|V_{zz}(\beta_2)|$ and that efg's of sites α and τ are significantly smaller. In Sec. VII, experimental efg ratios will be used to estimate the relative charges of A atoms, B atoms, and vacant sites.

III. SAMPLE PREPARATION

Samples of Ni_2Al_3 phases were made by weighing out desired quantities of the alloy constituents, placing carrier-free ^{111}In activity on the transition metal, wrapping the trivalent metal within the transition metal, and melting under argon in a small arc furnace. Sample masses were about 80 mg and compositions were determined typically to within 0.2 at. % after taking into account small mass losses that occurred during melting. Prior to PAC measurements, samples were annealed for 1 h in order to equilibrate the Ni_2Al_3 phase and promote crystal growth, after which the samples were cooled slowly to room temperature.

Samples having between 38 and 42 at. % of transition metal were made to determine how solute site preferences depend on composition. While Ni_2Al_3 has a phase field extending between about 38 and 42 at. % Ni (Ref. 9), the other two aluminides and two gallides appear as "line" compounds in binary phase diagrams.[13] Thus, some measurements were undoubtedly made on samples containing small amounts of other phases, but in which the dominant volume fraction was still of the Ni_2Al_3 phase. In previous work in this laboratory, the partition of dilute ^{111}In probes between two phases in a mixture was studied through measurement of site fractions of quadrupole interaction signals characteristic of each phase.[16] It was found that solutes may have a strong tendency to segregate to one or other of the two phases. To guard against misinterpreting signals from other phases as being from sites in the Ni_2Al_3 phase, PAC measurements were made in several neighboring phases, including $NiAl_3$, Pd_8Al_{21}, and Pt_3Ga_7 with results reported below. With the possible exception of a signal in Pt_2Ga_3, described below, no signals were observed in Ni_2Al_3 phases that could be attributed to a neighboring phase, including signals for ^{111}In/Cd probes with neighboring Ni vacancies in NiAl (Refs. 17 and 18) and NiGa (Ref. 19) that have been measured in this laboratory. (Measurements were not made on Ni_3Ga_4 and Ni_3Al_4 phases because they only order after annealing times of many weeks.[20])

IV. PERTURBED ANGULAR CORRELATION

In general, an angular correlation exists between directions of emissions of successive nuclear radiations. When the intermediate nuclear state is long lived, its nuclear moments can precess through appreciable angles due to the interaction with fields present at the nuclear site. This leads to a time-dependent perturbation of the angular correlation that can be measured using delayed coincidence techniques. The present measurements employed a well-known γ-γ cascade in ^{111}Cd, observed following decay of ^{111}In by electron capture with a mean life of four days. Emission of the first γ ray (173 keV) signals formation of an intermediate 247 keV level, with spin 5/2 and a mean life of 120 ns. Emission of the second (247 keV) γ ray signals decay to the ground state. During the lifetime of the intermediate state, the quadrupole moment interacts with the electric-field gradient at the nuclear site caused by all the external charges in the crystal. The present measurements were made on polycrystalline samples, for which there is an isotropic distribution of efg orientations over the ensemble of probe nuclei, in which case the correlation function for emission of radiations is given in good approximation by

$$W(\theta,t) = 1 + A_2 \gamma_a P_2(\cos\,\theta) G_2(t). \tag{2}$$

Here, θ is the angle subtended by detectors of the start (173 keV) and stop (247 keV) γ rays with respect to the sample, t is the time after formation of the intermediate state when it decays, A_2 is the anisotropy of the decay ($=-0.18$), γ_a is an angular attenuation coefficient that accounts for finite solid angles subtended by the detector, and $P_2(\cos\,\theta)$ is a Legendre polynomial. $G_2(t)$ is the perturbation function and contains all information about the interaction of nuclear moments with fields. For spin 5/2, the static perturbation function for quadrupole interaction when the efg has axial symmetry is

$$G_2(t) = \tfrac{1}{5}[1 + \tfrac{13}{7}\cos(\omega_1 t) + \tfrac{10}{7}\cos(2\omega_1 t) + \tfrac{5}{7}\cos(3\omega_1 t)], \tag{3}$$

in which the fundamental quadrupole interaction frequency ω_1 is given in term of the quadrupole moment Q of the nucleus and principal component of the efg tensor V_{zz} by

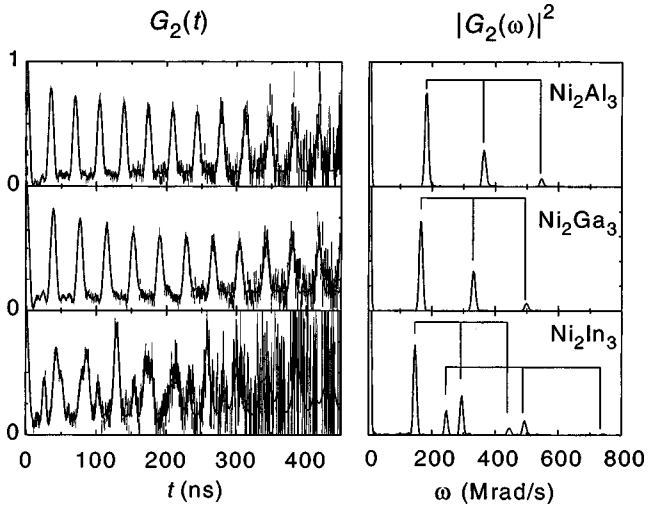

FIG. 4. PAC spectra of indium probes in Ni-rich Ni_2Al_3 and Ni_2Ga_3 and in Ni_2In_3 (left) and frequency power spectra obtained by Fourier transformation (right). The spectrum for Ni_2In_3 exhibits two quadrupole interaction signals for probes on β_2 and β_1 sites. Spectra for Ni_2Al_3 and Ni_2Ga_3 each exhibit only one quadrupole interaction signal whose frequency corresponds to that of the lower frequency β_2 site in Ni_2In_3.

$$\omega_1 = \frac{3\pi}{10}|eQV_{zz}|/h. \tag{4}$$

It can be seen from Eq. (3) that the perturbation function has three nonzero frequency harmonics and is periodic, with a characteristic shape shown, for example, in Fig. 4 (top). Distributions of distant defects or lattice strains may produce weak efg's that lead to inhomogeneous broadening of the perturbation function given in Eq. (3); this was fitted satisfactorily using a "damped" perturbation function having the form

$$\begin{aligned} G_2(t) = \tfrac{1}{5}\{1 &+ \tfrac{13}{7}\cos(\omega_1 t)\exp[-\tfrac{1}{2}(\sigma t)^p] \\ &+ \tfrac{10}{7}\cos(2\omega_1 t)\exp[-\tfrac{1}{2}(2\sigma t)^p] \\ &+ \tfrac{5}{7}\cos(3\omega_1 t)\exp[-\tfrac{1}{2}(3\sigma t)^p]\}, \end{aligned} \tag{5}$$

in which σ is a frequency distribution width and p controls the shape of the damping.

Measurements were carried out using a spectrometer with four BaF_2 scintillation detectors located in a plane surrounding the sample at angles of 90°. The typical time to accumulate a spectrum was one day. Multiple coincidence spectra of the general form $C(\theta,t)=\exp(-t/\tau_{nuc})W(\theta,t)+B$, in which $\exp(-t/\tau_{nuc})$ is a lifetime decay function and B is an accidental background, were collected at angles π and $\pi/2$ and combined to obtain the experimental perturbation function using the four-spectrum conventional ratio described in Ref. 21. When more than one ensemble of nuclei were present in a measurement, such as when solutes occupied several lattice sites, the experimental spectrum was fitted to a superposition of perturbation functions with amplitudes equal to the site fractions f_i of probes in each local environment; that is,

$$G_2 = \sum_i f_i G_2(\omega_i, t). \tag{6}$$

For further background and details about measurement methods, the reader is referred to Refs. 22–25.

Perturbation functions for nearly all spectra of Ni_2Al_3 phases could be fitted well using the amplitudes of the frequency harmonics appropriate for random efg orientations, given in Eq. (3). Deviations of amplitudes were observed in a few measurements that were attributed to nonrandom crystalline texture [e.g., in Fig. 14 (top) shown below]. However, such deviations were small and do not affect conclusions reached below.

PAC measurements were all made at room temperature. Because there was no atomic mobility in the time scale of the measurements, observed solute site preferences are those of the indium parent probes while quadrupole interactions are measured in Cd daughter nuclei. Site occupations were measured on samples in quenched states following slow cooling to room temperature in an annealing oven. Taking into consideration the cooling rate in the oven, measured site occupations are believed to represent equilibrium distributions of solutes and intrinsic defects at temperatures of order 200 −400 °C.

V. RESULTS

Table III summarizes quadrupole interactions observed in all Ni_2Al_3 phases at room temperature, with attributions of the sites explained below. PAC measurements have been previously reported for the indides Ni_2In_3 (Ref. 26), Pd_2In_3 (Ref. 27), and Pt_2In_3 (Ref. 28) with quadrupole interaction parameters very close to those observed in the present study. Results are presented first for transition-metal rich gallides and aluminides, then for transition-metal poor gallides, and finally for transition-metal poor aluminides. Supporting measurements on non-Ni_2Al_3 phases are also briefly described.

A. Strong preference for site β_2 in transition-metal rich gallides and aluminides

Figure 4 shows PAC spectra measured for Ni-rich Ni_2Al_3 and Ni_2Ga_3 at top and middle. For reference, a spectrum for Ni_2In_3 is shown at bottom, in which, of course, the host probe ^{111}In must occupy the β_1 and β_2 sites with site fractions of 1/3 and 2/3. Time domain PAC spectra are shown on the left and corresponding frequency power spectra obtained by Fourier transformation on the right. The power spectra exhibit frequency triplets corresponding to each site occupied. As expected, the Ni_2In_3 spectrum exhibits two signals with corresponding quadrupole frequencies of 244.8(8) and 145.8(3) Mrad/s and a ratio of site fractions close to 0.50 (visible as a ratio of 0.25 in the power spectrum). They are therefore attributed to indium probes on sites β_1 and β_2, respectively, with a frequency ratio $\omega_1(\beta_1)/\omega_1(\beta_2) = |V_{zz}(\beta_1)/V_{zz}(\beta_2)| = 1.679$. In contrast, spectra for Ni_2Al_3 and Ni_2Ga_3 each exhibit only one signal whose frequency is close to that of site β_2 in Ni_2In_3, with any other signals having site fractions less than or of the order of the detection limit of 1%. We conclude that indium has a strong preference

TABLE III. Room-temperature quadrupole interaction frequencies ω_1 and frequency distribution widths σ in Mrad/s, with site attributions. Unlisted widths are about 2 Mrad/s. Blank entries indicate nonobservation of signals for those sites.

Phase A_2B_3 site attribution	Transition-metal rich		Transition-metal poor		
	β_1	β_2	α	τ	Lattice sink (e.g., grain boundary)
Ni_2Al_3		180.7 (1)			130 (σ=80)
Pd_2Al_3		174.4 (1)			135 (σ=115), 103(1)
Pt_2Al_3		181.4 (2)			35 (σ=10)
Ni_2Ga_3		164.8 (3)	0(3)	18(2)[a]	
Pt_2Ga_3		171.3 (1)	16(1) or 0[b]	16(1) or 0[b]	
Ni_2In_3	244.8 (8)	145.8 (3)			
Pd_2In_3	244.0 (3)	154.4 (1)			
Pt_2In_3	263.9 (6)	169.1 (3)			

[a]Site fraction observed to peak near the stoichiometric composition.
[b]Identification of 0 and 16 Mrad/s signals is uncertain (see text).

for the β_2 site in both the Ni-rich aluminide and gallide.

Analogous results were obtained for transition-metal rich Pd and Pt phases. Figure 5 exhibits spectra measured for Pd-rich Pd_2Al_3 and for Pd_2In_3 (a Pd_2Ga_3 phase does not exist), and Fig. 6 spectra for Pt-rich Pt_2Al_3, Pt_2Ga_3, and Pt_2In_3. Like Ni_2In_3, Pd and Pt indides exhibit two signals having site fractions of about 1/3 and 2/3 and frequencies similar to those observed in Ni_2In_3. Ratios of frequencies of the two β sites for the Pd and Pt indides are 1.580 and 1.561, close to but somewhat lower than the value 1.679 observed for Ni_2In_3. The two aluminides and one gallide each exhibit only one signal whose frequency is close to that of the β_2 site in the indides and is therefore attributed to that site.

Figure 7 compares quadrupole interactions frequencies measured in TM-rich phases by plotting them as a function of the inverse volume of the unit cell. Because of the r^{-3} dependence, efg's for corresponding sites should fall on lines through the origin, thereby accounting for differences in lattice parameters. The frequencies fall in two distinct groups. The three frequencies for probes on β_1 sites in the indides form one group and the eight others form a second group, including β_2 signals of the indides. Because of the tight clustering of frequencies of the second group, we attribute all of them to probes on β_2 sites. The frequencies in each group fall remarkably close to the two drawn lines. In the context of the efg calculations, this suggests that absolute magnitudes of effective charges of corresponding atoms and vacancies in the different compounds are equal to each other within about 10%. To summarize results of this section, indium solute atoms exhibit a strong preference for site β_2 in all the transition-metal rich aluminides and gallides, a result that is consistent with the larger volume of that site, discussed above.

B. Switching from β_2 to α and τ sites in gallides as a function of composition

Measurements were made on Ni_2Ga_3 samples having compositions in the range 37.4–41.4 at. % Ni. Figure 8 com-

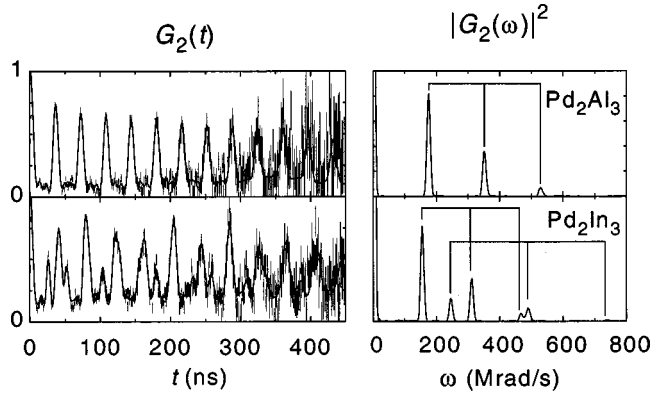

FIG. 5. PAC spectra of indium probes in Pd-rich Pd_2Al_3 and in Pd_2In_3 (left) and frequency power spectra (right). As in Fig. 4, the Pd_2In_3 spectrum exhibits two quadrupole interaction signals identified with sites β_2 and β_1. The single signal observed in Pd_2Al_3 is identified with indium solutes on site β_2.

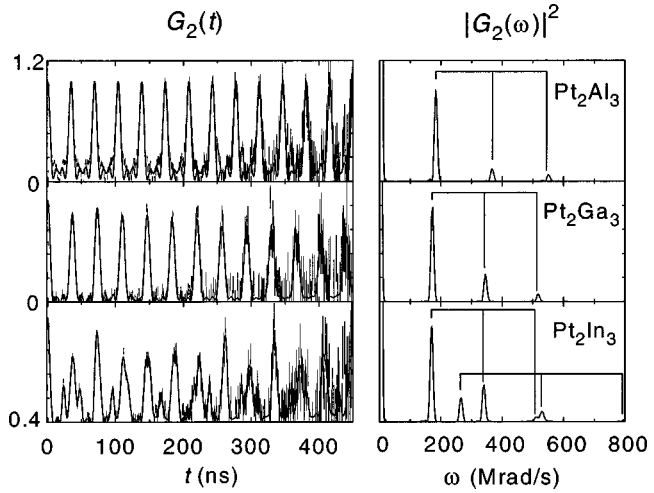

FIG. 6. PAC spectra of indium probes in Pt-rich Pt_2Al_3 and Pt_2Ga_3 and in Pd_2In_3 (left) and frequency power spectra (right). As in Fig. 4, the Pt_2In_3 spectrum exhibits two quadrupole interaction signals identified with sites β_2 and β_1. The single signals observed for Pt_2Al_3 and Pt_2Ga_3 are identified with solutes on site β_2.

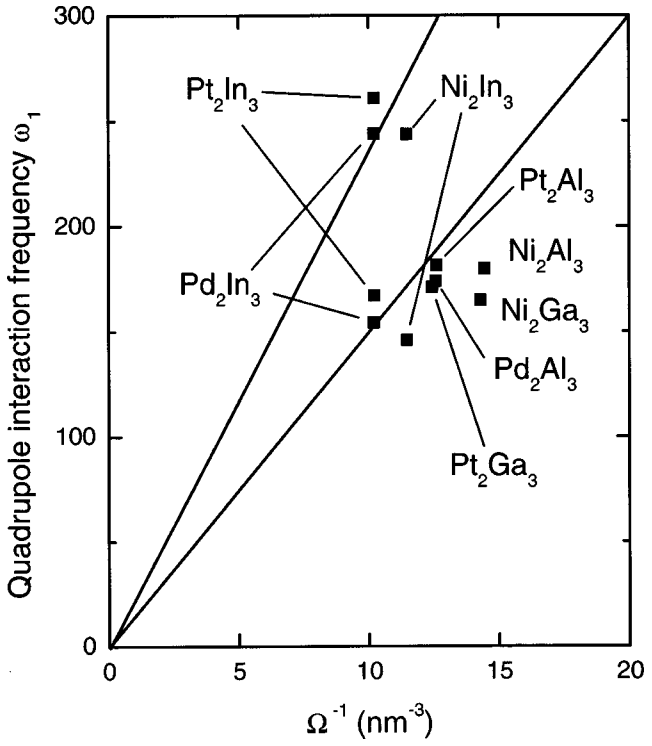

FIG. 7. Quadrupole interaction frequencies for In/Cd probes on β sites in Ni_2Al_3 phases. Frequencies are plotted vs the inverse of the unit-cell volume to account for differences in lattice parameters. For the indides, signals are observed for both sites β_1 (upper points) and β_2 (lower points) whereas the gallides and aluminides each exhibit only one signal attributed to site β_2.

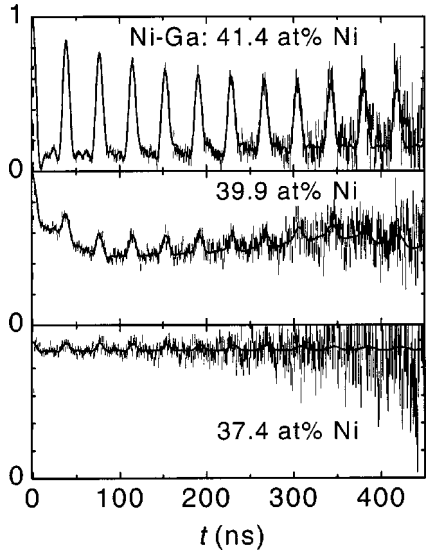

FIG. 8. PAC spectra for Ni_2Ga_3 samples. The spectrum for a Ni-rich sample (top) exhibits a signal of high frequency (165 Mrad/s) identified with site β_2. The Ni-poor spectrum shown at bottom exhibits a large site fraction of a signal with zero frequency. The spectrum for a stoichiometric sample exhibits the zero-frequency signal, the 165 Mrad/s signal, and also a 15 Mrad/s signal.

pares spectra for compositions that are Ni rich (top), stoichiometric (middle), and Ni poor (bottom). As can be seen the character of the spectra changes almost completely over that range of composition. The spectrum for the Ni-rich sample exhibits only the 164.8 Mrad/s signal attributed above to probes on the β_2 site. The spectrum for 37.4 at. % Ni exhibits primarily a zero-frequency signal, with only 5% of indium remaining on site β_2. The spectrum for 39.9 at. % Ni has a site fraction of about 60% for the zero-frequency signal, 20% for the β_2 signal, and 20% for a low-frequency 18(2) Mrad/s signal. The 0 and 18 Mrad/s signals have small frequency distribution widths, like signals for solutes on sites β_1 and β_2, indicating good crystal perfection.

Figure 9(a) shows how the three site fractions in Ni_2Ga_3 vary with composition. [Figure 9(b) shows a simulation that will be discussed below.] Several features can be observed.

(1) As the composition of Ni decreases and crosses the stoichiometric composition, the 165 Mrad/s signal from site β_2 is replaced mostly by the zero-frequency signal. The switchover occurs mostly within a range of composition equal to 1 at. %.

(2) The 18 Mrad/s signal has a maximum site fraction of about 20% near the stoichiometric composition and decreases for compositions on either side. Concerning the identification of the 0 and 18 Mrad/s signals, it can be recalled from the discussion of efg calculations that efg's for solutes on the α and τ sites are each expected to be small in comparison with efg's for sites β_1 or β_2. Thus it is natural to attribute the two low-frequency signals observed here to indium solutes on sites α and τ, although it is not possible to identify which signal belongs to which site because of uncertainty in the efg calculations and possible disturbance of efg's caused by local relaxation around the Cd probes.

It will be shown below using a thermodynamic model that the composition dependences of the site fractions are explained by assigning the 0 and 18 Mrad/s signals, respectively, to solutes on sites α and τ.

While Ni_2Ga_3 appears as a line compound in binary phase diagrams,[13] Fig. 9 shows that solute site fractions continue to change up to compositions of about 41.0(5) at. % Ni, indicating that the Ni-rich phase boundary is at or above 40.5 at. % Ni. In good approximation, the concentration of structural point defects increases linearly with the deviation from stoichiometry. Structural defects in Ni_2Ga_3 and the other Ni_2Al_3 phases produce weak efg disturbances that lead to inhomogeneous broadening that increases with the concentration of defects. Such broadening can be readily seen in the spectrum for 41.4 at. % Ni shown in Fig. 8 (top).

Limited measurements were carried out for Pt_2Ga_3, with spectra shown in Fig. 10 for two compositions. The β_2 signal that dominates for the Pt-rich sample is partially replaced in the Pt-poor sample by signals with zero frequency and a frequency of 16 Mrad/s. While these trends are analogous to those observed for Ni_2Ga_3, a 16 Mrad/s signal was also observed in spectra of the neighboring phase Pt_3Ga_7. We conservatively conclude that some indium transfers to either one or both the α and τ sites in Pt-poor Pt_2Ga_3, but additional measurements are needed. To summarize results of this section, the two gallides exhibit a common behavior with respect to dilute indium solutes; indium strongly prefers the β_2

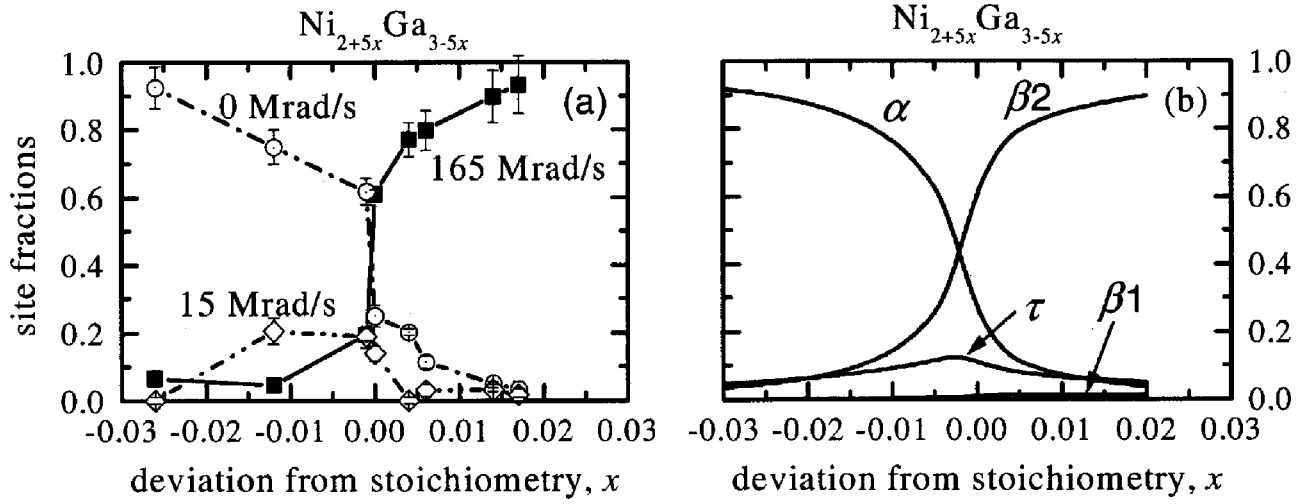

FIG. 9. Variations of the site fractions of 165, 0, and 15 Mrad/s signals in $Ni_{2+5x}Ga_{3-5x}$ with the deviation from stoichiometry, x, attributed, respectively, to indium solutes on α, β_2, and τ sublattices. Experimental data are shown at left, with a simulation shown at right made using a thermodynamic model described in the text.

site in Ga-poor samples and α and/or τ sites in Ga-rich samples.

C. Switching from β_2 to lattice-sink sites in aluminides

Figure 11 exhibits representative PAC spectra for indium probes in Ni_2Al_3 samples with Ni-rich, stoichiometric, and Ni-poor compositions. At the stoichiometric composition, only the 181 Mrad/s signal attributed to indium on site β_2 is observed, with a small frequency distribution width. At 42.0 at. % Ni, the same signal is observed with a larger frequency distribution width that is attributed to a greater concentration of structural point defects. Such defects could in principle be Ni atoms on τ or β sites or vacancies on β sites. At 42.0 at. % Ni, the concentrations would be very high (from 3.3% to 8% depending on the type of structural defect) easily leading to efg disturbances that could account for the amount of broadening observed.

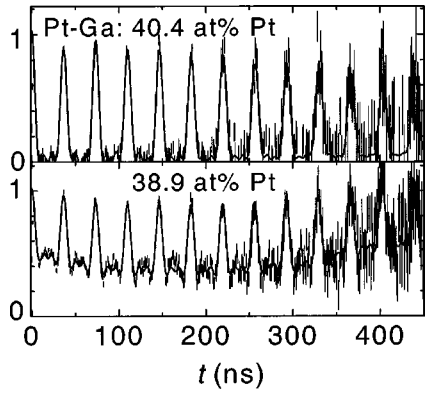

FIG. 10. PAC spectra for Pt_2Ga_3 samples. The spectrum for a Pt-rich sample (top) exhibits only a signal of frequency 171 Mrad/s identified with site β_2. The spectrum for a Pt-poor sample (bottom) exhibits a smaller site fraction of the 171 Mrad/s signal and signals having frequencies of 0 and 16 Mrad/s.

In spectra of Ni-poor Ni_2Al_3, the 181 Mrad/s signal is replaced mostly be a quadrupole interaction signal having a mean frequency of about 130 Mrad/s and large frequency distribution width (80 Mrad/s) (Fig. 11, bottom). This signal is visible in the figure as the rapid drop near $t=0$ and undershoot at $t\approx 20$ ns. Variations of the two site fractions with composition are displayed in Fig. 12, with curves showing results of a simulation that will be discussed below. (The figure also shows a ~2% site fraction of a low-frequency signal that is ignored in the following discussion). As can be

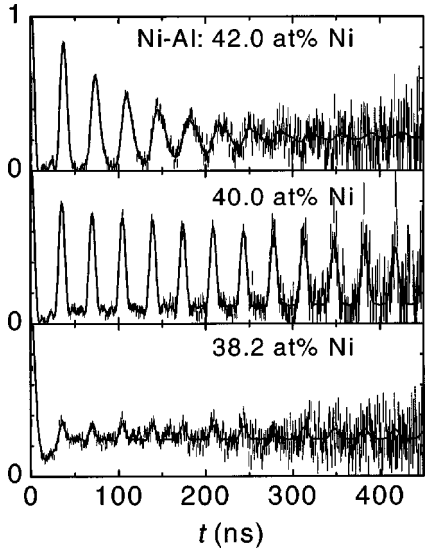

FIG. 11. PAC spectra for Ni_2Al_3 samples. The spectrum for the sample with a stoichiometric composition (middle) exhibits mostly a 181 Mrad/s signal attributed to indium on site β_2. For a Ni-rich sample (top) one observes the same signal with a greater frequency distribution width that is attributed to the presence of structural point defects at off-stoichiometric compositions. For a Ni-poor sample (bottom) only a small site fraction of the 181 Mrad/s signal is observed, having been replaced mostly by an extremely broadened signal with mean frequency of about 150 Mrad/s.

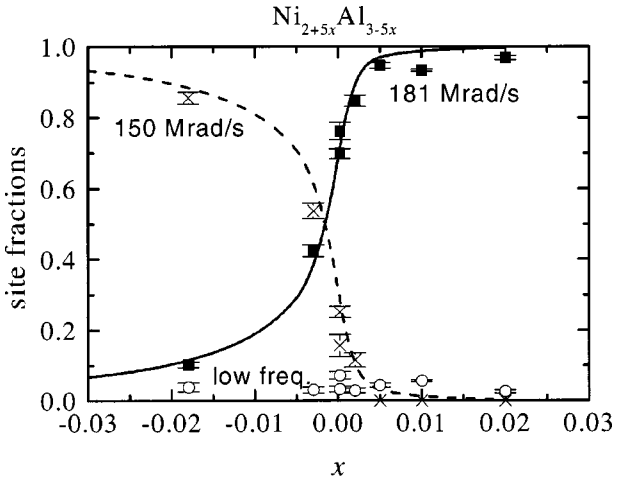

FIG. 12. Variation of site fractions of a 181 Mrad/s signal and inhomogeneously broadened 150 Mrad/s signal in $Ni_{2+5x}Al_{3-5x}$ with the deviation from stoichiometry x. The signals are attributed in the text to solutes on the β_2 sublattice and in lattice sinks, respectively. The curves drawn in the figure are from a simulation made using a thermodynamic model.

seen, the site fractions cross over in a range of composition of about 1 at. % near the stoichiometric composition. To identify the 130 Mrad/s signal, we first note that the frequency distribution of the 181 Mrad/s signal, visible with a small site fraction, remains narrow in the Ni-poor sample (bottom), indicating that the crystal structure remains well ordered. In addition, the frequency distribution width of the 130 Mrad/s signal was observed to be independent of composition, indicating that it is characteristic of the site (or sites) occupied and is not a function of defect concentrations. Consequently, the large distribution of the 130 Mrad/s signal must be attributed to sites other than regular lattice sites, such as sites in grain boundaries or dislocations, collectively termed lattice sinks. We conclude that indium solutes switch from the β_2 site in Ni-rich alloys to lattice-sink sites in Ni-poor alloys.

A similar behavior was observed for Pd_2Al_3 and Pt_2Al_3, with representative spectra shown in Figs. 13 and 14. The Pd-rich spectrum in Fig. 13 exhibits the 174 Mrad/s (β_2) signal with modest line broadening attributed to structural defects in the same way as for Ni_2Al_3 since the stoichiometric sample exhibits a signal with very little broadening. In the spectrum for the Pd-poor sample, the 174 Mrad/s signal has been completely replaced by two signals: one with a mean frequency of 135 Mrad/s and broad distribution width, σ=115 Mrad/s, and the other a 103 Mrad/s signal with small broadening. The 135 Mrad/s signal is equivalent in all respects to the 150 Mrad/s signal in Ni_2Al_3 and is likewise attributed to probes on lattice-sink sites. The 103 Mrad/s signal was not observed in adjacent phases and is attributed to the Pd_2Al_3 phase. The possibility that the 103 Mrad/s signal arises from probes on the α or τ sublattices is rejected because the efg would be much larger than anticipated on the basis of the efg calculations. An alternative possibility is that the 103 Mrad/s signal is a well-defined signal for probes in grain boundaries. While one generally expects grain boundaries to have many different sites available for solutes, leading to a large efg distribution, polygonization of the boundaries may lead to low-energy terraces on which solutes come to rest in a site with a unique local environment and efg. Such a well-defined signal has been observed in polycrystalline platinum.[29] We presume that the 103 Mrad/s site arises in this way.

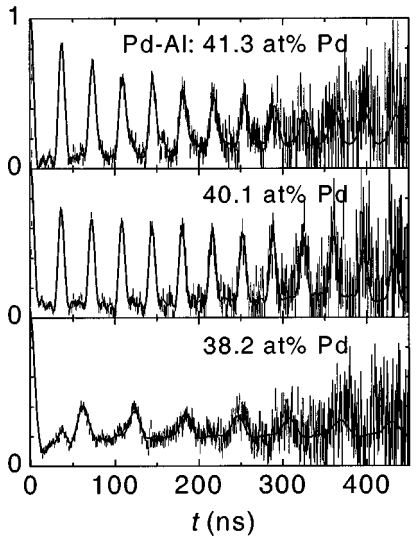

FIG. 13. PAC spectra for Pd_2Al_3 samples. The spectrum for the sample with a stoichiometric composition (middle) exhibits a 174 Mrad/s signal attributed to indium on site β_2. The Pd-rich sample (top) exhibits the same signal with an increased frequency distribution width attributed to structural point defects. The Pd-poor sample (bottom) exhibits only a small fraction of the 174 Mrad/s signal, having been replaced by an extremely broadened signal with mean frequency of about 135 Mrad/s and an unbroadened 103 Mrad/s signal. The 135 and 103 Mrad/s signals are attributed to solutes in lattice-sink sites.

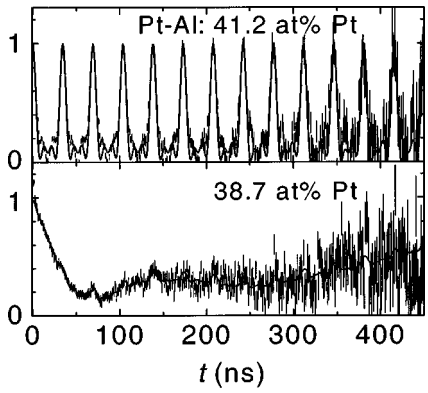

FIG. 14. PAC spectra for Pt_2Al_3. The spectrum for the Pd-rich sample (top) exhibits a very homogeneous 181 Mrad/s signal attributed to solutes on the β_2 sublattice. In the spectrum for the Pd-poor sample, the 181 Mrad/s signal has been almost completely replaced by an inhomogeneously broadened signal having a mean frequency of 35 Mrad/s that is attributed in the text to solutes in lattice-sink sites. High homogeneity of the signal at top suggests that the upper phase boundary of Pt_2Al_3 is very close to the stoichiometric composition.

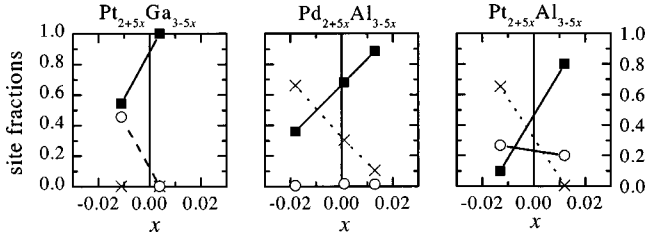

FIG. 15. Variations of site fractions of indium solutes with deviations from stoichiometry x in $Pt_{2+5x}Ga_{3-5x}$, $Pd_{2+5x}Al_{3-5x}$, and $Pt_{2+5x}Al_{3-5x}$ alloys. Solutes are predominantly on the β_2 sublattices in TM-rich alloys (squares) but on other sites in TM-poor alloys having zero or low frequency signals (circles) or highly inhomogeneous signals (crosses).

Pt_2Al_3 spectra are shown in Fig. 14 and exhibit the 181.4 Mrad/s (β_2) signal for the Pt-rich composition. For the Pt-poor composition, one observes a very small amount of the 181.4 Mrad/s signal, with small broadening, and a signal with mean frequency of 35 Mrad/s and broad width (σ=10 Mrad/s). Based on the small broadening of the 181.4 Mrad/s signal in the Pt-poor sample, it is concluded that there are few structural defects and that the large broadening is characteristic of the site having the 35 Mrad/s signal, in the same way as in Ni_2Al_3 and Pd_2Al_3. Consequently, the 35 Mrad/s signal is attributed to probes in lattice-sink sites. An additional aspect of the spectra gives qualitative information about the upper phase boundary of Pt_2Al_3. As can be seen, the 181.4 Mrad/s signal for the sample with 41.2 at. % Pt exhibits very little frequency broadening, in contrast to the larger broadening of the 181 Mrad/s signal in Ni-rich Ni_2Al_3, leading us to conclude that the concentration of any structural defects must be much smaller in 41.2 at. % Pt_2Al_3. From this, it is estimated that the upper phase boundary of Pt_2Al_3 must be very close to the stoichiometric composition, so that the 41.2 at. % Pt-Al sample consists of a mixture of Pt_2Al_3 and PtAl phases.

To summarize results of this section, the three aluminides exhibit a common behavior. Indium solutes strongly prefer site β_2 in TM-rich alloys and (unlike in gallides) lattice-sink sites in TM-poor alloys. Expressed differently, the solid solubility of indium in the crystal structure of TM-poor aluminides can be said to be less than or about one atom in 10^9. Figure 15 summarizes the observed dependences of site fractions in Pt_2Ga_3, Pt_2Al_3, and Pt_2Al_3 on nominal compositions. In these phases as well as Ni_2Ga_3 and Ni_2Al_3, indium solutes switch from the β_2 sublattice in TM-rich alloys to other sites in TM-poor alloys.

D. Measurements for neighboring phases

To test whether observed signals arose from probes in non-Ni_2Al_3 phases, PAC measurements were made on $NiAl_3$, Pd_8Al_{21}, and Pt_3Ga_7, with spectra shown in Fig. 16. Samples were prepared in the same way as the Ni_2Al_3 samples and annealed prior to measurement at room temperature. In Table IV are sample compositions, measured quadrupole interaction parameters ω_1 and η and comments about sites occupied by indium solutes in those compounds. With the possible exception of a 16 Mrad/s signal in Pt_2Ga_3, none of the Ni_2Al_3 phases exhibited spectral parameters observed in these compounds.

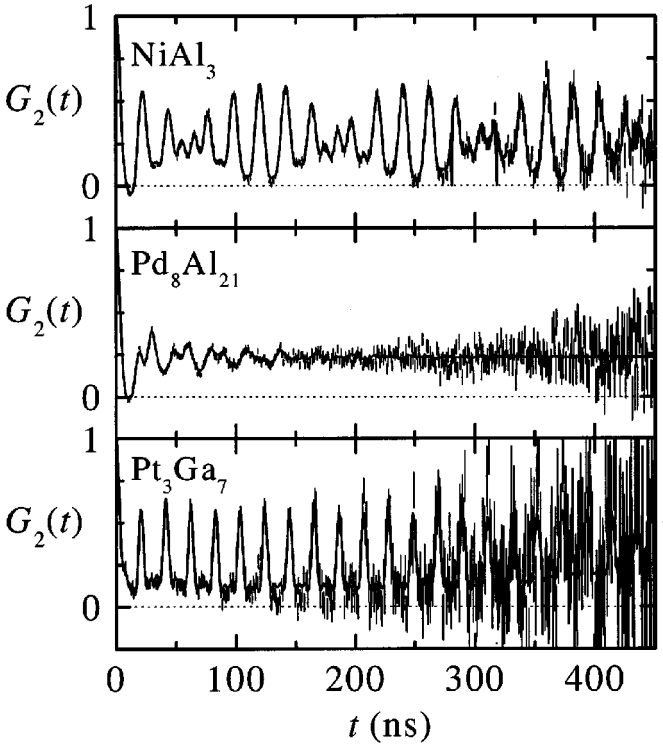

FIG. 16. PAC spectra of ^{111}In/Cd probes in $NiAl_3$, Pd_8Al_{21}, and Pt_3Ga_7.

It is noteworthy that strong site preferences were observed in two of the non-Ni_2Al_3 compounds. For slightly Ni-rich $NiAl_3$, only one signal was observed, which had a nonzero asymmetry parameter, and is attributed to indium on only one of two inequivalent Al sites. For Pd_8Al_{21}, the spectrum could be fitted to a superposition of six signals, so that indium probes occupy most of the eight distinct lattice sites in that compound and there is no strong site preference. For Pt_3Ga_7, signals were observed for two out of three possible sites.

VI. THERMODYNAMIC MODEL OF SITE-SELECTION BEHAVIOR

A thermodynamic model for the equilibrium partition of solute atoms among different sublattices was developed to interpret the observed behavior. Conceptually, equilibrium is established through reactions in which the solute atom transfers from one sublattice to another, accompanied by formation or dissolution of intrinsic point defects. In the Appendix, the thermodynamics of defects and solutes in the Ni_2Al_3 structure is derived starting from an expression for the free energy of the crystal under the usual assumption that defects are noninteracting. The derivation leads to mass-action-like expressions among defect concentrations that are applied in this section to obtain expressions for site fractions as a function of composition and temperature. It is further shown in the Appendix how to calculate concentrations of intrinsic

TABLE IV. Quadrupole interactions and lattice locations of indium in other phases.

Phase	Structure	Composition	ω_1(Mrad/s)	η	Indium solute lattice sites occupied
$NiAl_3$	CFe_3	25.07 (4) at. %Ni	262.4(1)	0.7918 (4)	Ni rich: one of three sites (probably one of two Al-sites)
Pd_8Al_{21}	Ge_8Pd_{21} (γ phase)	29.0 (2) at. %Pd	137 (2)	0.697 (35)	Pd-rich: six sites out of eight
			216 (2)	0.730 (15)	
			234 (1)	0.323 (10)	
			304 (2)	0.883 (9)	
			371 (3)	0.214 (20)	
			411 (2)	1.0	
Pt_3Ga_7	Ge_7Ir_3	30.2 (1.3) at. %Pt	303.2 (1)	0	Near stoichiometry: two of three sites plus one broadly distributed site
			16 (2)	~0	
			140 (σ=60)		

defects based on formation energies of the elementary intrinsic defects.

The full set of intrinsic defects in the Ni_2Al_3 structure (written generically as A_2B_3 in the following) includes vacancies on the three substitutional sublattices V_α, $V_{\beta 1}$, and $V_{\beta 2}$ (in which subscripts identify sublattice sites), antisite atoms $A_{\beta 1}$, $A_{\beta 2}$, and B_α, and interstitial atoms occupying the normally empty sublattice, A_τ and B_τ. For simplicity, it will be assumed in the following that vacancies $V_{\beta 1}$ and $V_{\beta 2}$ have the same energy and antisite atoms $A_{\beta 1}$ and $A_{\beta 2}$ have the same energy. This reduces the number of distinct intrinsic point defects to six (V_α, V_β, A_β, B_α, A_τ, and B_τ). In contrast, solute species $S_{\beta 1}$ and $S_{\beta 1}$ are allowed to have different energies, so that four distinguishable solute defects may be observed (S_α, $S_{\beta 1}$, $S_{\beta 2}$, and S_τ). Defect concentrations are defined as mole fractions on the corresponding sublattices and indicated by defect symbols in square brackets, e.g., $[V_\beta]$. With this definition, concentrations lie between physical limits of 0 and 1.

Mechanisms that equilibrate the solute among the sublattices can be written heuristically as exchange or transfer reactions. A solute atom S may equilibrate between sublattices α and β_2 via the generalized exchange reaction

$$S_a + X_{\beta 2} \leftrightarrow S_{\beta 2} + X_\alpha, \tag{7}$$

in which the species X stands for A, B, or V. Under the usual assumption for metallic systems that defects are noninteracting, the condition for equilibrium of Eq. (7) can be written in the form of a mass-action relation[30,31] among concentrations of the reactant and product species, with equilibrium constant $K_{\alpha\beta 2}$ given by

$$K_{\alpha\beta 2} = \frac{[S_{\beta 2}][X_\alpha]}{[S_\alpha][X_{\beta 2}]} = \exp(-G_{\alpha\beta 2}/k_B T), \tag{8}$$

in which $G_{\alpha\beta 2}$ will be called the free energy of transfer and is comprised of an enthalpy and entropy of transfer:

$$G_{\alpha\beta 2} \equiv H_{\alpha\beta 2} - TS_{\alpha\beta 2}. \tag{9}$$

Note that the value of $G_{\alpha\beta 2}$ will depend on whether $X=A$, B, or V. The method described in the Appendix leads to identifications of $G_{\alpha\beta 2}$ in terms of formation energies of defect and solute species. For $X=A$, for example, it is found that

$$G_{\alpha\beta 2}(X=A) = g^S_{\beta 2} - g^S_\alpha + g^A_{\beta 2}, \tag{10}$$

and for $X=V$

$$G_{\alpha\beta 2}(X=V) = g^S_{\beta 2} - g^S_\alpha + g^V_{\beta 2} - g^V_\alpha, \tag{11}$$

in which g^X_δ is the change in energy of the crystal when defect or solute species X replaces the normal occupant on the generic site δ (the normal occupant of the empty sublattice τ being a vacancy).

The ratio of site fractions on the α and β_2 sublattice, which can be compared directly with experiment, is obtained directly from Eq. (8):

$$\frac{f_{\beta 2}}{f_\alpha} = \frac{[S_{\beta 2}]}{[S_\alpha]} = \frac{[X_\beta]}{[X_\alpha]} \exp(-G_{\alpha\beta 2}/k_B T) \tag{12}$$

in which, again, $X=A$, B, or V, so that three alternative expressions are implied. Ratios of site fractions for other pairs of sites can be written similarly, except that one must account for different numbers of sites on the sublattices. For example, sublattices τ and β_2 have a 1:2 ratio of sites, so that

$$\frac{f_{\beta 2}}{f_\tau} = 2\frac{[S_{\beta 2}]}{[S_\tau]} = 2\frac{[X_\beta]}{[X_\tau]} \exp(-G_{\beta 2\tau}/k_B T). \tag{13}$$

For inequivalent sublattices of an element, such as β_1 and β_2 in the Ni_2Al_3 structure, the expression for the site-fraction ratio takes on a simpler form that does not involve defect concentrations. The exchange reaction

$$S_{\beta 1} + B_{\beta 2} \leftrightarrow S_{\beta 2} + B_{\beta 1} \tag{14}$$

leads to the site-fraction ratio

$$\frac{f_{\beta 2}}{f_{\beta 1}} = 2\frac{[S_{\beta 2}]}{[S_{\beta 1}]} = 2\ \exp(-G_{\beta 1\beta 2}/k_B T) \tag{15}$$

since in the limit of low defect concentrations, $[B_{\beta 1}] \cong [B_{\beta 2}] \cong 1$. The free energy of transfer is simply $G_{\beta 1\beta 2} = g^S_{\beta 2} - g^S_{\beta 1}$, the difference of energies of the solute in the two sites. An Arrhenius plot of the site-fraction ratio given in Eq.

(15) will exhibit linear behavior, independent of defect concentrations and therefore independent of the deviation from stoichiometry.

Arrhenius plots of other site-fraction ratios will not generally be linear. Consider the ratio $f_{\beta 2}/f_{\alpha}$:

$$\frac{f_{\beta 2}}{f_{\alpha}} = \frac{[S_{\beta 2}]}{[S_{\alpha}]} = [A_{\beta}]\exp[-(g^{S}_{\beta 2} - g^{S}_{\alpha} + g^{A}_{\beta 2})/k_B T]. \quad (16)$$

As shown in the Appendix, $[A_{\beta}]$ and other defect concentrations have complex temperature dependences in general, leading to nonlinear Arrhenius plots. There are two special cases in which the plots will be linear. (1) When the composition is strictly stoichiometric, then $[A_{\beta}]$ will be thermally activated with a well-defined activation enthalpy. (2) When the composition is far removed from stoichiometry, then the concentration of structural A_{β} will be much greater than the concentration of thermally activated A_{β}, and $[A_{\beta}]$ in Eq. (16) will be independent of temperature.

Solving for $[S_{\beta 2}]/[S_{\alpha}]$ in the three alternative expressions of Eq. (8) for $X=A$, B, and V leads to relations among defect and host-atom concentrations,

$$\frac{[A_{\alpha}]}{[A_{\beta}]} = c_1(T)\frac{[B_{\alpha}]}{[B_{\beta}]} = c_2(T)\frac{[V_{\alpha}]}{[V_{\beta}]}, \quad (17)$$

in which the c's are functions only of temperature. At a given temperature and in the approximation that defect concentrations are small so that one may take $[A_{\alpha}] \cong [B_{\beta}] \cong 1$, one obtains proportionalities $[A_{\beta}]^{-1} \propto [B_{\alpha}] \propto [V_{\alpha}]/[V_{\beta}]$ that apply for any composition. Similar proportionalities involving concentrations of interstitial defects can be obtained starting from expressions analogous to Eqs. (7)–(9) for solute exchange between substitutional and interstitial sites. One finds $[A_{\tau}]^{-1} \propto [V_{\alpha}] \propto [B_{\alpha}]/[B_{\tau}]$ and $[B_{\tau}]^{-1} \propto [V_{\beta}] \propto [A_{\alpha}]/[A_{\tau}]$.

Using the proportionalities among defect concentrations, it can be shown that any site-fraction ratio can be expressed in a power of the concentration of a selected defect species on either of the two sublattices. For a compound of arbitrary stoichiometry $A_m B_n$, there are four alternative expressions for the ratio of site fractions of a solute on sublattices β and α, for example,

$$\begin{aligned}\frac{f_{\beta}}{f_{\alpha}} &= \frac{n}{m}\frac{[S_{\beta}]}{[S_{\alpha}]} = \frac{n}{m}[A_{\beta}]\exp(-G_a/k_B T) \\ &= \frac{n}{m}[B_{\alpha}]^{-1}\exp(-G_b/k_b T) \\ &= \frac{n}{m}[V_{\alpha}]^{-(m+n)/n}\exp(-G_c/k_B T) \\ &= \frac{n}{m}[V_{\beta}]^{(m+n)/m}\exp(-G_d/k_B T), \end{aligned} \quad (18)$$

in which the G's are defined in terms of the free energies of the intrinsic defects and solutes, as outlined in the Appendix. The four concentration-dependent factors in Eq. (18) are shown in the Appendix to be monotonically increasing functions of the A content of the alloy, so that the site fraction ratio f_{β}/f_{α} must likewise increase monotonically with the A content.

One can now outline qualitative trends in site preference behavior. The site fractions themselves are obtained from a complete set of the site-fraction ratios and, returning to the Ni_2Al_3 structure, one has, for example,

$$f_{\beta 2} = \frac{1}{1 + f_{\beta 1}/f_{\beta 2} + f_{\alpha}/f_{\beta 2} + f_{\tau}/f_{\beta 2}}. \quad (19)$$

$f_{\beta 2}$ will be large if and only if all ratios in the denominator are small compared to 1 and will be small if any ratio in the denominator is large. To examine how site fractions vary with composition, it is useful to express site-fraction ratios appearing in Eq. (19) in terms of the product of a defect concentration and a thermally activated factor. Using Eq. (18) to obtain $f_{\beta 2}/f_{\alpha}$ and corresponding equations for other ratios, one obtains

$$f_{\beta 2} = \frac{1}{1 + \frac{1}{2}e^{+G_{\beta 1 \beta 2}/k_B T} + e^{+G_{\alpha \beta 2}/k_B T}[B_{\alpha}] + \frac{1}{2}e^{+G_{\tau \beta 2}/k_B T}[B_{\tau}]}, \quad (20)$$

in which the free energies of transfer G depend on formation energies of elementary defects. Using methods described in the Appendix, $G_{\beta 1 \beta 2} \equiv g^{S}_{\beta 2} - g^{S}_{\beta 1}$, $G_{\alpha \beta 2} \equiv g^{S}_{\beta 2} - g^{S}_{\alpha} + g^{B}_{\alpha}$, and $G_{\tau \beta 2} \equiv g^{S}_{\beta 2} - g^{S}_{\tau} + g^{B}_{\tau}$. It is important to note that the transfer energies G in general depend not only on the differences of site energies of the solute but also on the formation energy of an intrinsic defect or defects. Let us write the composition of the sample as $A_{2+5x}B_{3-5x}$, in which x measures the deviation from stoichiometry. As shown in the Appendix, both $[B_{\alpha}]$ and $[B_{\tau}]$ must decrease monotonically with increasing x, so that, as expressed in Eq. (20), $f_{\beta 2}$ can only increase with x. The same result is obtained for $f_{\beta 1}$.

Reasoning similarly, one obtains for the site fraction on the other host element sublattice, f_{α},

$$f_{\alpha} = \frac{1}{1 + (\frac{1}{2}e^{+G_{\alpha \beta 1}/k_B T} + e^{+G_{\alpha \beta 2}/k_B T})[A_{\beta}] + \frac{1}{2}e^{+G_{\tau \beta 1}/k_B T}[A_{\tau}]}. \quad (21)$$

Since $[A_{\beta}]$ and $[A_{\tau}]$ increase monotonically with x, f_{α} can only decrease with x. Thus, Eqs. (20) and (21) show that fractions of solute on substitutional sites increase monotonically as the amount of host element normally on that site decreases.

For the interstitial site fraction f_{τ}, one obtains, in contrast,

$$f_{\tau} = \frac{1}{1 + (e^{+G_{\tau \beta 1}/k_B T} + 2e^{+G_{\tau \beta 2}/k_B T})[V_{\beta}] + 2e^{+G_{\tau \alpha}/k_B T}[V_{\alpha}]}. \quad (22)$$

Since $[V_{\beta}]$ and $[V_{\alpha}]$ must increase and decrease respectively with increasing x, f_{τ} tends to have a maximum value near the stoichiometric composition, where both concentrations are normally least. Naturally, if either of the terms involving $[V_{\beta}]$ or $[V_{\alpha}]$ in the denominator of Eq. (22) is much less than 1 for all compositions, then the predominant site fraction

may change from interstitial to substitutional as the stoichiometric composition is crossed.

Lattice-sink sites can also be included in a site-occupation model using exchange reactions.[34] For example, the reaction for a solute S switching with species X between sublattice $\delta(\delta=\alpha,\beta1,\beta2)$ and a lattice-sink site is

$$S_\delta + X_{\text{sink}} \leftrightarrow S_{\text{sink}} + X_\delta, \tag{23}$$

in which X_{sink} denotes a sink site normally occupied by an X atom ($X=A$ or B). Defining the equilibrium constant in the same way as in Eq. (8), the site-fraction ratio is found to be

$$\frac{f_{\text{sink}}}{f_\delta} = \frac{R[S_{\text{sink}}]}{[S_\delta]} = \frac{R[X_{\text{sink}}]}{[X_\delta]} \exp(-G_{\delta\text{sink}}/k_BT), \tag{24}$$

in which the inserted constant R is the ratio of the number of sites in the sink to the number on sublattice δ and is proportional to the sink density. The site-fraction ratio in Eq. (24) will only depend on composition if X is the atom type not normally found on sublattice δ. Inclusion of lattice-sink sites leads to the appearance of additional terms in the denominators of Eqs. (19)–(22).

The concentrations of elementary defects appearing in Eqs. (20)–(22) are functions of temperature and composition that can be calculated as described in the Appendix. They can be calculated by solving polynomial equations such as Eq. (A12), which depend on equilibrium constants for formation of equilibrium defect combinations. An example of such a combination is the eight-defect $5A_\tau + 3B_\alpha$, for which the formation reaction and equilibrium constant K_8 are given in Eqs. (A8) and (A9). Five such combinations are sufficient to completely specify the polynomial equations. Other combinations are listed in the Appendix.

To simulate the observed switching of solutes from β_2 to sink sites in Ni_2Al_3 shown in Fig. 12, it had to be assumed that the solute transfers to an A-type sink site. To reduce the number of model parameters, Only A_τ and B_α were assumed to have appreciable concentrations, in accordance with experimental[32] and theoretical[33] results. With this assumption, one cannot use Eq. (23) because it involves $A_{\beta2}$ instead of A_τ and B_α. An alternative transfer reaction is $2A_\alpha + 3S_{\beta2} + 3A_{\text{sink}} \leftrightarrow 3S_{\text{sink}} + 5A_\tau$ with equilibrium constant $K_{\beta2\text{sink}}$. The curves drawn in Fig. 12 show results of a simulation with parameters $K_8 = 5.0\times10^{-19}$ and $K_{\beta2\text{sink}}R^2 = 3.0\times10^{11}$ and can be seen to reproduce the composition dependence well, including asymmetry in the crossover.

For Ni_2Ga_3, little is known about the intrinsic defects. A simulation of switching of solutes among, $\beta2$, α, and τ sites shown in Fig. 9(a) was carried out assuming all defects might be present in appreciable concentrations. This required more model parameters than in the simulation for Ni_2Al_3. Simulated site-fraction dependences shown in Fig. 9(b) were obtained using Eqs. (20)–(22) with the parameters $K_8 = 2.9\times10^{-25}$, $K_2 = 5.0\times10^{-6}$, $K_5 = 2.6\times10^{-32}$, $K_{2A} = 4.3\times10^{-6}$, $K_{2B} = 8.3\times10^{-12}$, $K_{\beta1\beta2} = 2.5\times10^{+1}$, $K_{\alpha\beta2}(X=A) = 8.5\times10^{+2}$, and $K_{\tau\beta2}(X=A) = 5.3\times10^{-1}$, with K_2, K_5, K_{2A}, and K_{2B} defined in the Appendix. As can be seen, the simulation reproduces switching of solutes between substitutional sublattices α and β_2 and peaking of the interstitial site fraction near the stoichiometric composition. In the present case, however, it is impossible to obtain a unique set of model parameters due to the large number of parameters and limited number of experimental observations. Knowledge about intrinsic defects would help reduce the number of model parameters (as illustrated in the simulation for Ni_2Al_3), and measurements as a function of temperature would help to extract enthalpy and entropy parameters from the equilibrium constants.

Site-selection behavior in Ni_2Al_3 phases was investigated more generally through a large number of simulations using the thermodynamic model for site occupations and defect concentrations outlined above and in the Appendix. Simulations were also made in which energies of antisite atoms and vacancies were allowed to differ according to which β sublattice they occupied, but no qualitatively new behavior was discovered. Depending on the values of the solute and defect energies g^X_δ, it was observed that a solute may reside principally on one sublattice for all compositions, switch between substitutional sublattices as the stoichiometric composition is crossed, or switch to an interstitial sublattice near the stoichiometric composition. For suitable ranges of energies, a solute may also be observed to switch between substitutional and interstitial sublattices as the stoichiometric composition is crossed. The qualitative behavior describing how solute site fractions depend on composition can be summarized in the following heuristic rules. At a given temperature we have the following.

(1) Solutes tend to occupy substitutional sites of an element in which there is a deficiency, that is, sites α in A-poor alloys and β in B-poor alloys. This is a consequence of the fact that site fractions on substitutional sites only vary monotonically as a function of composition. A simple explanation is that the total defect count is less when the solute is placed on the sublattice of the element in which there is a deficiency than when it is placed on the sublattice of an element with an excess.

(2) Solutes generally tend to occupy interstitial or empty-lattice sites maximally near the stoichiometric composition, with the site fraction decreasing for compositions to either side.

(3) Ratios of site fractions of solutes on inequivalent sublattices of one host element (or on inequivalent interstitial sublattices) are solely a function of temperature and are independent of the composition.

(4) Composition dependences of site fractions of solutes in lattice sinks may be quite varied. Site fractions may be large for $x>0$ and small for $x<0$ or *vice versa*, or be large or small for all compositions.[34] If interstitiallike sites also are present in sinks, then the site fractions may peak near the stoichiometric composition.

(5) These qualitative results are independent of the mode of disorder in a phase since, as shown, for example, in Eq. (18), a site-fraction ratio can be expressed in terms of any possible defects on the two sublattices. The results are also valid for a phase of general stoichiometry A_mB_n.

One can further investigate how site fractions vary with temperature. If one assumes for simplicity that a single thermally activated defect combination predominates, then its constituent elementary defects will be the structural defects observed for off-stoichiometric compositions at low tempera-

ture. For example, for the eight-defect $(5A_\tau + 3B_\alpha)$, the structural defects will be A_τ in *A*-rich samples and B_α in *B*-rich samples. At low temperature, essentially only structural defects will be present. Their concentrations will be negligible on one side of the stoichiometric composition and increase linearly on the other. Also at low temperature, the thermal factors in Eqs. (20)–(22) will be very large or small depending on the signs of the free energies of transfer *G*. Therefore, at low temperature, if a solute switches between two substitutional sites, the switch will be abrupt and occur very close to the stoichiometric composition. If a solute is favored to occupy an interstitial site, its site fraction may peak sharply at the stoichiometric composition at low temperature.

At intermediate temperatures, thermal activation of defects will elevate concentrations of defects above those at low temperature by greater amounts in the composition range close to stoichiometry. As a consequence, the existence of thermal defects will reduce the sharpness of switching near the stoichiometric composition. Simulations show that the range of composition over which a solute switches between substitutional sites, or occupies interstitial sites, increases linearly with absolute temperature. Finally, a solute may switch between substitutional sites as a function of temperature for some compositions but not others, depending on values of the set of g_δ^X's.

VII. DISCUSSION AND CONCLUSIONS

Effective charges of host atoms and empty sites. One can use experimental efg ratios for Ni_2Al_3 phases to estimate effective charge ratios for the host atoms and vacant sites, q_A/q_V, using Fig. 3. For ^{111}Cd probes, experimental ratios $|V_{zz}(\beta_1)/V_{zz}(\beta_2)|$ for the three indides Ni_2In_3, Pd_2In_3, and Pt_2In_3 are 1.679, 1.580, and 1.561, respectively (see Table III). Using Fig. 3, the average efg ratio 1.60(5) of the three indides corresponds to $q_A/q_V \cong +0.1$. Taking charge neutrality into account, this suggests that relative charges are in the proportions $q_A:q_B:q_V = -0.1:+0.4:-1$. Since the hyperfine Cd probe is an impurity, efg ratios might be modified by local lattice relaxation from those observed using host probes. However, a recent NMR measurement by Bastow and West[35] of quadrupole interactions in Ni_2In_3 yielded a ratio $|V_{zz}(\beta_1)/V_{zz}(\beta_2)| = 1.729$, in good agreement with the PAC value of 1.679. Thus, local lattice relaxation near Cd impurities does not have a major effect on efg ratios. From Fig. 3, the ratio 1.729 obtained using NMR implies $q_A/q_V \cong +0.3$, from which one obtains charges in similar proportions $q_A:q_B:q_V = -0.33:+0.5:-1$. For a ratio $|V_{zz}(\beta_1)/V_{zz}(\beta_2)| \cong 1.70$, Fig. 3 shows that efg's at sites α and τ are almost identically zero, a result consistent with measurements on Ni_2Ga_3 reported above. This increases confidence in the derived charge proportions. Since the vacancy's charge can only arise from a density of conduction electrons that overlaps the vacancy, it must be negative. The above proportions indicate that charges of *A* and *B* atoms must be negative and positive, respectively. This result is consistent with the greater electronegativity (or work functions[15]) of transition-metal atoms. It is curious that the vacant site has an effective charge greater in magnitude than of either host atom. No other data on effective charges are known for comparison.

Observed site-selection and site-switching behavior. Indium impurities were always observed to occupy site β_2 for TM-rich compositions in Ni_2Al_3 phases. This is consistent with the general rule that solutes tend to occupy sites of an element in which there is a deficiency. Of the two β sites, the β_1 site has six TM neighbors while the β_2 site has five. Assuming that the binding of indium increases with the number of bonding TM neighbors, one would expect indium to be more stable on site β_1. On the other hand, the β sites also differ in the available volume, with β_2 sites having Wigner-Seitz volumes that are $\approx$7.5% larger (as shown in Table II). The observed preference for site β_2 thus appears to reflect the greater importance of the volume misfit of the oversized indium solute.

As compositions changed from TM rich to TM poor, indium solutes in all five Ni_2Al_3 phases were observed to transfer from site β_2 to other sites. In the gallides, solutes transferred to sites with small efg's and narrow frequency distributions that were identified with sites α and τ. In the three aluminides, solutes transferred to sites with large, inhomogeneous efg's that were identified as lattice-sink sites such as in grain boundaries. The contrasting behaviors of TM-poor gallides and aluminides are attributed to differences in relative energies of indium solutes in lattice and sink sites.

Ranges of compositions over which solutes were observed to switch sites could be very narrow. For Ni_2Ga_3, the range in Fig. 9 is of order 0.1 at. %, whereas for Ni_2Al_3 in Fig. 12 it is somewhat broader, ~0.5 at. %. The ranges depend on the enthalpy of formation of the dominant defect combination, temperature, and solute concentration. We emphasize that in the experiments described here, solutes had mole fractions of the order of 10 parts per billion, so that solute concentrations were far below concentrations of dominant intrinsic defects. In general, the composition range over which site-switching behavior is observed will be broadened by an amount of the order of the solute concentration. Therefore, techniques requiring solute concentrations of the order of 1 at. %, such as x-ray diffraction or ALCHEMI, can be expected to exhibit more gradual changes in site occupation as a function of composition. The relatively steep changes observed in the present work are a consequence of the very low concentration of solute. We expect that PAC experiments carried out with higher solute concentrations would exhibit more gradual site-switching behavior.

The most interesting site observed was the low-frequency site in Ni_2Ga_3 with a maximum site fraction close to the stoichiometric composition. Such a maximum is only predicted for an interstitial, or empty-lattice, site. Such behavior has not to our knowledge previously been predicted or observed.

The present study focused on variation of site fractions in Ni_2Al_3 phases with composition. An attempt was also made to measure such variations with temperature, but without success. Elsewhere, we report on a study of the temperature dependence of solute site occupation in $GdAl_2$, in which indium solutes were observed to transfer from Gd sites at low temperature to Al sites at high temperature. A free energy of

transfer was determined from the temperature dependence of the ratio of site fractions, such as given by Eq. (12), for several different compositions.

Implications of the model and observations. The experiments and thermodynamic model demonstrate that locations of solutes in compounds can depend sensitively on the composition near stoichiometry. As a consequence, nominally equivalent measurements of site occupations may easily exhibit significant discrepancies or even contradictory results. Even a "line compound" with a phase field having a width of ~0.3% may exhibit quite varied site occupations, depending on the detailed composition and thermal history. In the present work, this was dramatically demonstrated for the phases Ni_2Ga_3, Pd_2Al_3, Pt_2Al_3, and Pt_2Ga_3, all of which appear as line compounds in binary phase diagrams[13] but which exhibit much different site fractions of indium solutes when prepared in such a way as to be TM rich or poor. To avoid ambiguity in the interpretation of measurements of site occupation, it is desirable to make measurements for a range of compositions and/or temperature.

The finding that interstitial or empty-lattice sites tend to be occupied by solutes near the stoichiometric composition does not appear to have been previously noted. The range over which an interstitial site fraction is large may be very sharply peaked at or near the stoichiometric composition in samples equilibrated at low temperature.

ACKNOWLEDGMENTS

This work was supported in part by the National Science Foundation under Grant No. DMR 00-91681 (Metals Program). We thank Bonner C. Walsh for assistance with some measurements.

APPENDIX

In this appendix, equilibria among defect and solute species in the Ni_2Al_3 structure are derived starting from a statistical mechanical description of the Gibbs free energy of the crystal. The perfect structure A_2B_3 is considered to have three substitutional sublattices, α, $\beta 1$, and $\beta 2$, occupied by A, B, and B atoms, and one empty, or interstitial, sublattice τ. Intrinsic defects include vacancies on the various substitutional sublattices V_α, $V_{\beta 1}$, $V_{\beta 2}$, antisite atoms $A_{\beta 1}$, $A_{\beta 2}$, B_α, and interstitials A_τ, B_τ. A solute species S may locate on one or more of the four sublattices: S_α, $S_{\beta 1}$, $S_{\beta 2}$, and S_τ.

In metals, coulomb interactions among defects and solutes are reduced by screening of the conduction electrons. It will be assumed accordingly that defects and solutes are noninteracting, in which case the free energy of the crystal can be written[30] as

$$\begin{aligned} G = {} & Ng_0 + N_\alpha^B g_\alpha^B + N_\alpha^V g_\alpha^V + N_{\beta_1}^V g_{\beta 1}^V + N_{\beta 1}^V g_{\beta 1}^V + N_{\beta 2}^A g_{\beta 2}^A \\ & + N_{\beta 2}^V g_{\beta 2}^V + N_\tau^A g_\tau^A + N_\tau^B g_\tau^B + N_\alpha^S g_\alpha^S + N_{\beta 1}^S g_{\beta 1}^S + N_{\beta 2}^S g_{\beta 2}^S \\ & + N_\tau^S S_\tau^S - TS_{config}, \end{aligned} \tag{A1}$$

in which N_δ^X is the number of atoms or defects of type X on sublattice δ, N is the total number of unit cells, and g_0 is the Gibbs free energy per unit cell of the perfect crystal. g_α^B is the change in free energy of the crystal that occurs when a B_α defect is formed, and similarly for the other defects and for solutes. Each g can be written in terms of a formation enthalpy and vibrational formation entropy: $g_\delta^X = h_\delta^X - Ts_\delta^X$. The configurational entropy $S_{config} \equiv k_B \ln \Omega$ is given in terms of the number of ways Ω in which defects and solutes can be arranged at random on the various sublattices:

$$\Omega = \frac{N_\alpha ! \, N_{\beta 1} ! \, N_{\beta 2} ! \, N_\tau !}{N_\alpha^A ! \, N_\alpha^B ! \, N_\alpha^V ! \, N_\alpha^S ! \, N_{\beta 1}^B ! \, N_{\beta 1}^A ! \, N_{\beta 1}^V ! \, N_{\beta 1}^S ! \, N_{\beta 2}^B ! \, N_{\beta 2}^A ! \, N_{\beta 2}^V ! \, N_{\beta 2}^S ! \, N_\tau^V ! \, N_\tau^A ! \, N_\tau^B ! \, N_\tau^S !}. \tag{A2}$$

Equilibrium values of N_δ^X are obtained by minimizing the crystal Gibbs free energy with respect to N_δ^X, subject to structural and compositional constraints. Consistent with the structure of Ni_2Al_3, total numbers of sites on the four sublattices are in the proportions

$$N_\alpha : N_{\beta 1} : N_{\beta 2} : N_\tau = 2:1:2:1. \tag{A3}$$

The solute concentrations will be assumed to be negligible in comparison with those of the principal intrinsic defects, in which case one finds from Eq. (A3), for example,

$$N_\alpha^A + N_\alpha^B + N_\alpha^V = 2(N_\tau^A + N_\tau^B + N_\tau^V), \tag{A4}$$

with analogous equations involving other pairs of sublattices. If the composition is assumed fixed at $A_{2+5x}B_{3-5x}$, in which x marks the deviation from stoichiometry, then the ratio of the total numbers of A and B atoms is

$$\frac{N^A}{N^B} \equiv \frac{N_\alpha^A + N_{\beta 1}^A + N_{\beta 2}^A + N_\tau^A}{N_{\beta 1}^B + N_{\beta 2}^B + N_\alpha^B + N_\tau^B} = \frac{2 + 5x}{3 - 5x}. \tag{A5}$$

For simplicity, it will be assumed below that $g_{\beta 1}^V = g_{\beta 2}^V$ and $g_{\beta 1}^A = g_{\beta 2}^A$. As a consequence, fractional concentrations of vacancies on the two β sublattices are equal and concentrations of antisite atoms on the two β sublattices are equal. This simplification is easily removed for a complete treatment.

Equilibrium concentrations are found by minimizing the crystal Gibbs free energy subject to the constraints given by Eqs. (A3)–(A5). This is accomplished by the method of Lagrange multipliers, which leads to a set of coupled equations involving defect and solute concentrations. Host atom, defect, and solute concentrations will be defined as fractional concentrations on the sublattices and written in square brackets so that, for example, for the number N_α^V of vacancies on

the α sublattice out of a total number of sites N_α, $[V_\alpha] \equiv N_\alpha^V/N_\alpha$. Elimination of the multipliers among the above equations leads to a large set of equations involving defect and solute concentrations.

Some equations in the set do not involve solutes and represent formation of defect combinations that can be created without altering the composition of the phase. For example, one such equation describes formation of the antisite pair:

$$K_2 = \frac{[A_\beta][B_\alpha]}{[A_\alpha][B_\beta]} = \exp(-(g_\beta^A + g_\alpha^B)/k_BT) = \exp(-G_2/k_BT), \tag{A6}$$

in which K_2 is the equilibrium constant. The pair can be considered to arise via the exchange reaction

$$A_\alpha + B_\beta \leftrightarrow A_\beta + B_\alpha. \tag{A7}$$

As an alternative to the above approach that uses Lagrange multipliers, one can obtain a set of equations for formation of defect combinations by inspection using the law of mass action familiar from chemical thermodynamics.[30,31] A modest benefit obtained by starting from Eqs. (A1)–(A5) is that the free energies of reaction, such as $G_2 = g_\beta^A + g_\alpha^B$ in Eq. (A6), are clearly defined in terms of defect and solute energies.

To determine concentrations of intrinsic defects, one must consider mass-action equations of a complete set of defect combinations. Five defect combinations are sufficient to establish equilibria among the six elementary defects in the Ni_2Al_3 structure. The combinations are pairings of structural defects on opposing sides of the stoichiometric composition: that is, a combination of V_α, B_α or B_τ (for *B*-rich alloys) with V_β, A_β, or A_τ (for *A*-rich alloys). One such combination is the antisite pair described above. Another is the eight-defect,

$$3A_\alpha \leftrightarrow 5A_\tau + 3B_\alpha, \tag{A8}$$

in which a unit cell disappears as the reaction goes from left to right. Heuristically, the reaction can be realized in steps: inserting the two *A* atoms and three *B* atoms from a unit cell into the interstices and then exchanging three *A* atoms on the α sublattice with the three interstitial *B* atoms. The corresponding mass-action equation is

$$K_8 = \frac{[A_\tau]^5[B_\alpha]^3}{[A_\alpha]^3} = \exp(-(5g_\tau^A + 3g_\alpha^B - g_0)/k_BT) = \exp(-G_8/k_BT). \tag{A9}$$

To complete the set of five defect combinations, one can choose the Schottky-like defect, obtained by removing a molecule to the surface and leaving behind five vacancies, $2V_\alpha + 3V_\beta$, and two types of Frenkel defects, $A_\tau + V_\alpha$ and $B_\tau + V_\beta$. Equilibrium constants for the five combinations will be written below in an obvious notation as K_2, K_8, K_5, K_{2A}, and K_{2B}, respectively.

To calculate an individual defect concentration, it is most convenient to start from a general equation of constraint among the defect concentrations. We restrict ourselves to the dilute solute limit. Inserting the set of structural constraints [Eq. (A4) and similar equations] into the compositional constraint [Eq. (A5)] leads to the following general relation among defect concentrations in a Ni_2Al_3 phase of composition $A_{2+5x}B_{3-5x}$:

$$2[B_\alpha] + (\tfrac{6}{5} - 2x)[V_\alpha] + (\tfrac{2}{5} + x)[B_x] + 5x = [A_{\beta 1}] + 2[A_{\beta 2}] + (\tfrac{2}{5} + x)([V_{\beta 1}] + 2[V_{\beta 2}]) + (\tfrac{3}{5} - x)[A_x]. \tag{A10}$$

With the above assumption that concentrations of intrinsic defects on sublattices β_1 and β_2 are equal and an additional assumption that the deviation from stoichiometry is small, $x \ll 1$, Eq. (A10) simplifies to

$$2[B_\alpha] + \tfrac{6}{5}[V_\alpha] + \tfrac{2}{5}[B_x] + 5x = 3[A_\beta] + \tfrac{6}{5}[V_\beta] + \tfrac{3}{5}[A_x]. \tag{A11}$$

In the approximation of small defect concentrations, $[A_\alpha] \cong [B_\beta] \cong [V_\tau] \cong 1$, mass-action equations for formation of the five defect combinations such as given in Eqs. (A6) and (A9) can be substituted in Eq. (A11) to obtain a polynomial equation in a power of any specified defect concentration. For example, Eq. (A11) leads to the following equation that can be readily solved to obtain $[A_\tau]$ for given values of x and all the K's:

$$3\frac{K_2}{K_8^{1/3}}[A_\tau]^{10/3} + \frac{3}{5}[A_\tau]^{8/3} + \frac{6}{5}\frac{K_5^{1/3}}{K_{2A}^{2/3}}[A_\tau]^{7/3} - 5x[A_\tau]^{5/3} - \frac{2}{5}\frac{K_{2B}}{K_5^{1/3}}K_{2A}^{2/3}[A_\tau] - \frac{6}{5}K_{2A}[A_\tau]^{2/3} - 2K_8^{1/3} = 0. \tag{A12}$$

It can be seen from Eq. (A12) that $[A_\tau]$ is a monotonically increasing function of x. Similarly, $[A_\beta]$ and $[V_\beta]$ increase and $[B_\tau]$, $[B_\alpha]$, and $[V_\alpha]$ decrease monotonically with increasing x.

Polynomial equations in defect concentrations can be simplified when knowledge is available about equilibrium defects. Experimental studies of Ni_2Al_3 by Taylor and Doyle[32] were interpreted to show that the structural defects are A_τ and B_α. The same defects were recently calculated to have the lowest formation energies using a FLAPW electronic structure program.[33] These findings lead to the expectation that the dominant thermally activated defect combination in Ni_2Al_3 is the eight-defect, in which case the formation energy per elementary defect of the eight-defect is less than the formation energies per defect of the other combinations. Assuming that the only non-negligible defect concentrations are $[B_\alpha]$ and $[A_\tau]$, Eq. (10) reduces to

$$2[B_\alpha] + 5x = (\tfrac{3}{5} - x)[A_\tau], \tag{A13}$$

and upon elimination of $[B_\alpha]$ using Eq. (A9), one obtains the simple polynomial equation

$$(\tfrac{3}{5} - x)[A_\tau]^{8/3} - 5x[A_\tau]^{5/3} - 2K_8^{1/3} = 0, \tag{A14}$$

which can be solved as a function of composition (x) and temperature (via K_8).

Other equations that can be obtained using the method of Lagrange multipliers or by applying the law of mass action to transfer reactions such as given in Sec. VI involve concentrations of solutes and intrinsic defects. For example, the exchange reaction

$$S_\alpha + A_\beta \rightarrow S_{\beta 2} + A_\alpha \tag{A15}$$

leads to

$$K_{\alpha\beta 2} = \frac{[S_{\beta 2}][A_\alpha]}{[S_\alpha][A_\beta]} = \exp(-(g^S_{\beta 2} - g^S_\alpha - g^A_\beta)/k_\beta T) = \exp(-G_{\alpha\beta 2}/k_B T), \tag{A16}$$

which was implicit in Eq. (8).

Finally, the above derivation was obtained assuming that concentrations of solute are negligible relative to intrinsic defects. One can generalize the equations of constraint given in Eqs. (A4) and (A5) in a straightforward way to include finite concentrations of solute.

*Email address: collins@wsu.edu

[1] See, e.g., M. Kogachi, Defect Diffus. Forum **121-122**, 15 (1995).
[2] See, e.g., I. M. Anderson, Acta Mater. **45**, 3897 (1997).
[3] H. G. Bohn, R. Schumacher, and R. J. Vianden, Mater. Res. Soc. Symp. Proc. **81**, 123 (1987).
[4] Gary L. Catchen, James M. Adams, and Todd M. Rearick, Phys. Rev. B **46**, 2743 (1992); Dunbar P. Birnie and Gary L. Catchen, J. Mater. Res. **8**, 1379 (1993).
[5] Matthew O. Zacate and Gary S. Collins, Hyperfine Interact. **136/137**, 647 (2001).
[6] Gary S. Collins and Matthew O. Zacate, Hyperfine Interact. **136/137**, 641 (2001).
[7] A. J. Bradley and A. Taylor, Proc. R. Soc. London, Ser. A **159**, 56 (1937).
[8] A. J. Bradley and A. Taylor, Philos. Mag. **23**, 1049 (1937).
[9] A. Taylor and N. J. Doyle, J. Appl. Crystallogr. **5**, 201 (1972).
[10] Y. Austin Chang and Joachim P. Neumann, Prog. Solid State Chem. **14**, 221 (1982).
[11] *Pearson's Handbook of Crystallographic Data for Intermetallic Phases*, 2nd ed., edited by P. Villars and L. D. Calvert (ASM International, Materials Park, OH, 1991).
[12] M. Ellner, U. Kattner, and B. Predel, J. Less-Common Met. **87**, 305 (1982)
[13] *Binary Alloy Phase Diagrams*, edited by T. B. Massalski (ASM International, Materials Park, OH, 1990).
[14] F. R. de Boer, R. Boom, W. C. M. Mattens, A. R. Miedema, and A. K. Niessen, *Cohesion in Metals: Transition Metal Alloys* (North-Holland, Amsterdam, 1988); H. Bakker, *Enthalpies in Alloys: Miedema's Semi-empirical Model* (Trans Tech Publications, Switzerland, 1998).
[15] Gary S. Collins and Matthew O. Zacate, Hyperfine Interact. **151**, 77 (2003).
[16] Matthew O. Zacate, Bonner C. Walsh, Luke S.-J. Peng, and Gary S. Collins, Hyperfine Interact. **136/137**, 653 (2001).
[17] Gary S. Collins, Praveen Sinha, and Mingzhong Wei, Hyperfine Interact. **C1**, 380 (1996).
[18] Matthew O. Zacate and Gary S. Collins, Defect Diffus. Forum **194-199**, 383 (2001).
[19] Gary S. Collins and Matthew O. Zacate (unpublished).
[20] M. Ellner, K. J. Best, H. Jacobi, K. Schubert, J. Less-Common Met. **19**, 294 (1969); M. Ellner, S. Kek, and B. Predel, *ibid.* **154**, 207 (1989).
[21] A. R. Arends, C. Hohenemser, F. Pleiter, H. De Waard, L. Chow, and R. M. Suter, Hyperfine Interact. **8**, 191 (1980).
[22] H. Frauenfelder and R. M. Steffen, in *Alpha-, Beta- and Gamma-Ray Spectroscopy*, edited by K. Siegbahn (North-Holland, Amsterdam, 1968).
[23] Günter Schatz and Alois Weidinger, *Nuclear Condensed Matter Physics* (John Wiley, New York, 1996).
[24] Gary S. Collins, Steven L. Shropshire, and Jiawen Fan, Hyperfine Interact. **62**, 1 (1990).
[25] Gary S. Collins and Praveen Sinha, Hyperfine Interact. **130**, 151 (2000).
[26] R. Platzer, U. Woehrmann, X. L. Ding, R. Fink, G. Krausch, J. Voight, R. Wesche, and G. Schatz, Hyperfine Interact. **60**, 1003 (1990).
[27] P. Wodniecki, B. Wodniecka, M. Marszalek, and A. Z. Hrynkiewicz, Hyperfine Interact. **80**, 1033 (1993).
[28] M. Marszalek, B. Wodniecka, P. Wodniecki, and A. Z. Hrynkiewicz, Hyperfine Interact. **80**, 1029 (1993).
[29] Bin Bai and Gary S. Collins, Hyperfine Interact. **79**, 761 (1993).
[30] A. R. Allnatt and A. B. Lidiard, *Atomic Transport in Solids* (Cambridge University Press, Cambridge, 1993), Chap. 3.
[31] L. E. Reichl, *A Modern Course in Statistical Physics* (University of Texas, Texas, 1980), Chap. 3.
[32] A. Taylor and N. J. Doyle, J. Appl. Crystallogr. **5**, 210 (1972).
[33] M. Weinert (private communication).
[34] Gary S. Collins and Matthew O. Zacate, Mater. Res. Soc. Symp. Proc. **719**, F8.19.1 (2002).
[35] T. J. Bastow and G. W. West, J. Phys.: Condens. Matter **15**, 8389 (2003).